*Article*

# The Synthesis of Cu–Mn–Al Mixed-Oxide Combustion Catalysts by Co-Precipitation in the Presence of Starch: A Comparison of NaOH with Organic Precipitants

Bogna D. Napruszewska, Anna Walczyk, Dorota Duraczyńska [ID], Joanna Kryściak-Czerwenka, Alicja Michalik, Robert Karcz [ID], Michał Śliwa [ID] and Ewa M. Serwicka *[ID]

Jerzy Haber Institute of Catalysis and Surface Chemistry, Polish Academy of Sciences, Niezapominajek 8, 30-239 Krakow, Poland
* Correspondence: ncserwic@cyf-kr.edu.pl; Tel.: +48-12-6395-118

**Abstract:** Cu–Mn mixed oxides are well known as active combustion catalysts. The common method for their synthesis is based on co-precipitation, with NaOH as a precipitant, and is burdened with the possibility of introducing undesired Na contamination. This work describes the use of two organic bases, tetrabutylammonium hydroxide and choline hydroxide, as precipitating agents in a novel alkali-free route for Cu–Mn–Al catalyst synthesis. To obtain fine crystalline precursors, which are considered advantageous for the preparation of active catalysts, co-precipitation was carried out in the presence of starch gel. Reference materials prepared with NaOH in the absence of starch were also obtained. Mixed oxides were produced by calcination at 450 °C. The precursors contained $MnCO_3$ doped with Cu and Al, and an admixture of amorphous phases. Those prepared in the presence of starch were less crystalline and retained biopolymer residues. The combustion of these residues during calcination enhanced the formation of larger amounts of the $Cu_{1.5}Mn_{1.5}O_4$ spinel phase, with better crystallinity in comparison to catalysts prepared from conventionally synthesized precursors. Tests of toluene combustion demonstrated that the catalysts prepared with starch performed better than those obtained in starch-free syntheses, and that the mixed oxides obtained by the alkali-free route were more active than catalysts prepared with NaOH. Catalytic data are discussed in terms of property–performance relationships.

**Keywords:** Cu–Mn mixed oxides; combustion catalyst; alkali-free synthesis; organic base; tetrabuty-lammonium hydroxide; choline hydroxide; starch; biotemplate; toluene combustion

## 1. Introduction

The pollution of air with volatile organic compounds (VOCs) represents a serious environmental hazard [1]. VOCs, i.e., carbon-based chemicals with a boiling point below 250 °C, are commonly used as solvents, cleaning products, fossil fuels, etc. The main sources of atmospheric contamination with VOCs are industrial and transportation activities, but indoor pollution may also stem from ingredients of commonly used household products. The emissions endanger human health due to the toxic, carcinogenic, and mutagenic nature of VOCs. In addition, upon sunlight irradiation, VOCs contribute to the formation of so-called photochemical smog, a toxic mixture of ozone and secondary organic aerosol (SOA) pollutants. The latter results chiefly from the photooxidation of primary VOCs; it may consist of ketones, aldehydes, alcohols, nitrates, or carboxylic acids [2–6].

Among many strategies aiming to control and mitigate VOC emissions, catalytic combustion is considered a particularly attractive clean-up technology as it enables the efficient, safe, and cost-effective purification of air [2–12]. In general, total oxidation catalysts are based either on noble metals or on transition metal oxides. The former show excellent activity but are costly and prone to poisoning by heteroatom-containing VOCs. On the other hand, oxide catalysts, most frequently containing Cu, Mn, Ce, Co,

Fe, Cr, etc. as active redox components, are significantly cheaper and less susceptible to deactivation by poisoning, but they usually display lower activity and require higher operating temperatures [2–12].

Among the large variety of catalytic formulations of oxide-type catalysts, the system combining oxides of Cu and Mn has a particularly long history, as it dates back to research on gas mask absorbents carried out in the U.S. during World War I. The mixtures of Cu and Mn oxides that were known under the general name hopcalite turned out to be extremely efficient in low-temperature CO oxidation [13,14]. Over the years, it transpired that catalysts based on the Cu–Mn–O system were also very active in the total oxidation of various VOCs, and research into this field has gained widespread interest (e.g., [15–36]). The high activity of mixed Cu–Mn oxides in total oxidation is generally attributed to the formation of copper manganite spinel phases, i.e., $CuMn_2O_4$ or solid solutions of $CuMn_2O_4$ and $Mn_3O_4$, described by the general formula $Cu_xMn_{3-x}O_4$ ($0 < x \leq 1$). It is argued that the co-existence of interacting $Cu^{2+}/Cu^+$ and $Mn^{4+}/Mn^{3+}$ redox couples, combined with the enhanced mobility of lattice oxygen in poorly crystalline spinel phases, are the chief factors responsible for the unique properties of hopcalite-related combustion catalysts [16,18,19,21–26,33].

Analysis of the literature data shows that the catalytic performance of mixed Cu–Mn oxides depends strongly on the preparation method, and a variety of synthetic approaches have been proposed. Different modifications of co-precipitation from Cu and Mn salt solutions by basic precipitants are the most frequently encountered preparation methods [15–18,20,21,23,27,35]. Redox precipitation using $KMnO_4$ as a source of Mn is another often-employed method of catalyst synthesis [18,27,29–31,33,37]. In some works, the impregnation of the Cu–Mn active phase on a support has been used [19,26]. Recently, highly active toluene combustion catalysts were obtained by a solid-state redox reaction between $Cu_2O$ and $MnO_2$ [36].

In order to better fit the requirements of the total oxidation reaction, synthesis procedures have been proposed that are aimed specifically at the diminution of precursor particles and achieve low crystallinity of the generated mixed-oxide catalysts. To this end, templating with the use of mesoporous silica [25,34] or alginate gel with anionic function [21,23] has been described, as well as synthesis by the water-in-oil inverse microemulsion method [15,28] or the low-temperature decomposition of tetraamminecopper (II) permanganate precursor [32]. However, all these routes involve elaborate, time-consuming procedures. Hard templating with mesoporous silica requires the preparation of a template and its removal from the final product by reactive dissolution; the alginate method is complicated by the necessity of hydrogel dehydration by a multistep solvent exchange; microemulsion syntheses are very laborious and difficult to upscale; and the synthesis of tetraamminecopper (II) permanganate involves a sequence of experimentally demanding intermediate steps.

In the search for a simpler method of obtaining nanocrystalline Cu–Mn precursors, we decided to investigate co-precipitation in the presence of starch as a biotemplating medium. Biotemplating is an effective synthetic strategy that enables the preparation of materials with a specific morphology and texture, thus impacting the related physicochemical properties [38]. The attractiveness of the approach is associated with the wealth of possible structure-directing templates, the feasibility of large-scale synthesis, and its satisfactory reproducibility. Starch is a cheap, abundant, renewable, and eco-friendly natural polysaccharide whose ability to undergo gelatinization, when heated in water, prompted applications as a soft biotemplate in the design of nanomaterials [39–42]. Recently, we studied the effect of starch addition on the co-precipitation of Mg–Al hydrotalcites and found that the use of a biotemplate unfailingly led to the preparation of less crystalline material [43,44].

Another aspect of synthesis studied in this work was the nature of the base reactant used for co-precipitation. As a rule, aqueous solutions of $Na_2CO_3$, $NaHCO_3$, and/or NaOH are used as precipitants. This may lead to contamination of the final product with

sodium residue unless the synthesis involves a very thorough washing of the precursor precipitate. It has been repeatedly pointed out that the presence of Na impurity may have a detrimental effect on the activity of a mixed-oxide catalyst, e.g., by decreasing its reducibility or accelerating the sintering of the active phase [45–49]. In general, the most straightforward way to prepare sodium-free mixed-oxide catalysts is by using $NH_3aq$ as a precipitating base. However, in the case of Cu-containing systems, the loss of the Cu component from the precipitate due to the formation of copper ammine complexes has to be considered. Einaga et al. [50] solved this problem by preparing Na-free Mn–Cu mixed-oxide catalysts using an organic base, i.e., tetramethylammonium hydroxide (TMAOH). This approach found few followers [26,35], probably because of the exceptional toxicity of TMAOH, whose proper handling requires extreme safety precautions [51]. We have recently demonstrated that other quaternary ammonium bases, such as tetrabutylammonium hydroxide (TBAOH) and choline hydroxide (ChOH), are excellent hydrolyzing agents for the co-precipitation of Mg–Al hydrotalcites [52].

In the present work, we carried out a comparative study of the effect of starch templating on the physicochemical properties of co-precipitated Cu–Mn–Al precursors and mixed oxides derived therefrom. The precursors were prepared with the use of three different bases as precipitants: NaOH, ChOH, and TBAOH. The catalytic performance of the calcined mixed oxides was tested in the combustion of toluene, a standard model compound of aromatic VOCs.

## 2. Results

### 2.1. Physicochemical Characterization

#### 2.1.1. XRD Analysis

Co-precipitation at a constant pH, adopted in this work for the preparation of precursors, is routinely employed for the synthesis of hydrotalcite-like materials [53]. Previously, we used this approach to synthesize Cu–Mn–Al hydrotalcite-like precursors of mixed oxides used as catalysts for methane combustion [23]. There, the molar amount of carbonate used in the synthesis was equal to the molar content of Al, i.e., it was twice the stoichiometric demand for the precipitation of the carbonate form of the Al-containing hydrotalcite structure. The synthesis resulted in the formation of a hydrotalcite-like phase with an admixture of $MnCO_3$. However, preliminary experiments carried out in this work showed that more active combustion catalysts could be derived from precursors co-precipitated in the presence of a larger carbonate excess, corresponding to twice the molar content of Al; therefore, all catalysts were synthesized in this manner.

The XRD patterns of precursors obtained with and without starch are shown in Figure 1a. It is obvious that irrespective of the nature of the precipitating base, the only detectable phase, or, in the case of P-NaOH, the dominating phase, is that of rhodochrosite, $MnCO_3$ (ref. code 01-084-6983). The average crystallite sizes calculated from the fwhm (full width at half maximum) of the most intense (104) plane reflection with the Scherrer formula are given in Table 1. For each precipitating base, the $MnCO_3$ crystallinity in materials obtained in the presence of the biotemplate is lower than in the counterparts prepared in starch-free syntheses. The result confirms that the use of a starch template hampers the crystallization of precipitated precursors. The additional reflections found in the XRD diagram of P-NaOH match well the positions of the most intense peaks in the Cu-containing hydrotalcite-like structure [Ref. code 46-0099]. Apart from the hydrotalcite-like admixture present in P-NaOH, there is no indication of other crystalline phases containing Cu and/or Al. However, a comparison of the position of the most intense (104) reflection in the synthesized samples with that in the $MnCO_3$ reference, which was prepared without copper or aluminum ions in the solution, shows that in the ternary systems, the peak maximum is shifted towards higher 2$\Theta$ values, indicating the contraction of the interplanar distance (Figure 1b). A similar effect observed previously in Cu–Mn precursors was attributed to the incorporation of copper into the $MnCO_3$ lattice [54,55]. In $MnCO_3$, the $Mn^{2+}$ ions assume a high-spin state [56], for which the ionic radius is 0.83 Å. The ionic radius of $Cu^{2+}$

is 0.73 Å. Thus, the observed shift in the (104) maximum position is consistent with the partial replacement of $Mn^{2+}$ with $Cu^{2+}$. In the ternary Cu–Mn–Al system, the incorporation of $Al^{3+}$ (ionic radius 0.54 Å) into the rhodochrosite lattice should also be considered. The $MnCO_3$ phase precipitated from Mn and Al salts with the exclusion of Cu shows a very small shift in the most intense peak with respect to pristine $MnCO_3$, suggesting that only a little substitution of Al for Mn occurred (Figure 1b). In fact, the incorporation of $Al^{3+}$ into the $MnCO_3$ structure is much more challenging than that of $Cu^{2+}$, due to the differences in the ionic charge and radius. For instance, the substitution of $Mn^{2+}$ with a trivalent cation would require the formation of structural defects, such as, e.g., $Mn^{2+}$ vacancies, to ensure lattice electroneutrality. However, this difficulty may be overcome in ternary Mn–Cu–Al systems, where the insertion of $Al^{3+}$ could be compensated by the simultaneous incorporation of $Cu^+$ (ionic radius 0.77 Å). Thus, it may be assumed that the rhodochrosite phase present in the synthesized precursors is doped by both copper and aluminum. The incorporation of foreign cations into $MnCO_3$ has a profound effect on its crystallinity. $D_{104}$ crystal sizes calculated for the ternary systems (Table 1) are lower by an order of magnitude than in the case of the $MnCO_3$ reference synthesized in the same conditions (56.9 nm). The shift of the (104) reflection is more pronounced in biotemplated precursors obtained with organic bases. This may be taken as an indication of a higher degree of Cu for Mn substitution in these less-ordered solids. According to Porta et al. [54], the $MnCO_3$ structure may host at most 30% $Cu^{2+}$; hence, the presence of a partially substituted $MnCO_3$ phase cannot account for all Cu introduced during synthesis. The absence of other crystalline phases implies that the lacking Cu, Al, and, possibly, Mn, exist in the form of amorphous phases, most likely of hydrotalcite-like, hydroxide, and/or carbonate type.
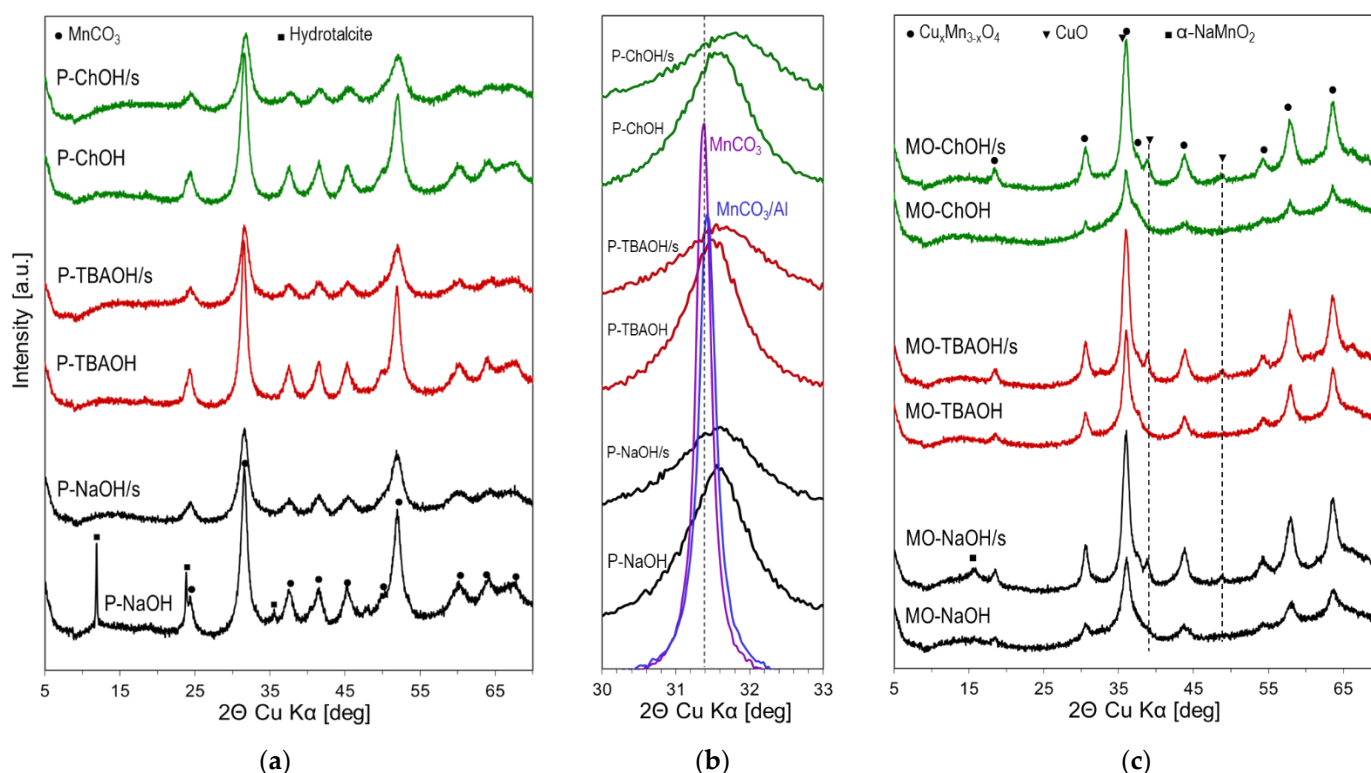


**Figure 1.** XRD patterns of: (**a**) precursors of mixed-oxide catalysts; (**b**) close-up of (104) reflection in, as received precursors, pristine $MnCO_3$ and $MnCO_3/Al$ (rhodochrosite phase obtained from mixed Mn–Al salt solution); (**c**) mixed oxides obtained by the calcination of precursors at 450 °C.

The XRD patterns of precursors calcined at 450 °C are gathered in Figure 1c. All samples show reflections attributable to the copper manganite spinel phase $Cu_xMn_{3-x}O_4$, with a structure best fitted to that of the $Cu_{1.5}Mn_{1.5}O_4$ formula (Ref. code 70-0260). The

position of XRD reflections is constant in all samples, pointing to the similar composition of the spinel phase in all calcined solids. EDX analysis confirms that the average Cu:Mn ratio in the prepared samples is close to the intended 1:2 (Table 1). This implies that not all Mn used in the synthesis enters the spinel structure. Gillot et al. [57] found that a spinel of nominal composition $CuMn_2O_4$ was unstable below 750 °C and existed as a mixture of a copper-rich $Cu_{1.5}Mn_{1.5}O_4$ form and $\alpha$-$Mn_2O_3$. In the present work, spinel is the only crystalline phase detectable in mixed oxides synthesized without starch, which points to the presence of an Mn-rich amorphous mixed-oxide component. In all materials prepared from starch-templated precursors, in addition to spinel features, low-intensity reflections pointing to the presence of some CuO (Ref. code 80-1268) can be seen. Moreover, in the XRD pattern of MO-NaOH/s, an additional peak at $2\Theta = 15.8°$ appears. Its position coincides with the most intense reflection of layered $\alpha$-$NaMnO_2$ (Ref. code 27-0752). Apparently, the presence of a significant amount of sodium residue in material prepared with NaOH in the presence of starch enabled the formation of this compound (Table 1). It is evident that the reflections of spinel phases in samples obtained from biotemplated precursors are more intense, which is indicative of a larger quantity of the spinel component in these samples. Due to the superposition of the most intense (311) spinel reflection, with the (002) reflection of CuO (both positioned around $2\Theta = 36°$), the (400) spinel reflection at $2\Theta = 43.7°$ was selected for comparison of spinel crystallinity. The application of the Scherrer formula to peak analysis shows that in biotemplated samples, the $D_{400}$ crystal sizes are 15–35% larger than in the counterparts prepared in starch-free syntheses (Table 1).

**Table 1.** Physicochemical parameters of synthesized solids: crystal sizes of rhodochrosite component in precursors ($D_{104}$) and the spinel phase in calcined mixed oxides ($D_{400}$). Also displayed: Cu, Mn, Al, and Na content in calcined mixed oxides, and C and N content in the precursors.

| Sample | $MnCO_3$ $D_{104}$ [nm] | Spinel $D_{400}$ [nm] | Cu [at. %] | Mn [at. %] | Al [at. %] | Na [at. %] | C [wt. %] | N [wt. %] |
|---|---|---|---|---|---|---|---|---|
| P-NaOH | 8.4 | - | - | - | - | - | 5.74 | 0.09 |
| P-NaOH/s | 6.7 | - | - | - | - | - | 17.04 | 0.17 |
| MO-NaOH | - | 7.2 | 24.9 | 48.6 | 24.0 | 2.5 | - | - |
| MO-NaOH/s | - | 8.3 | 24.2 | 47.8 | 23.4 | 4.6 | - | - |
| P-TBAOH | 8.5 | - | - | - | - | - | 7.76 | 0.37 |
| P-TBAOH/s | 6.4 | - | - | - | - | - | 18.56 | 0.52 |
| MO-TBAOH | - | 7.2 | 25.6 | 49.4 | 25.0 | 0 | - | - |
| MO-TBAOH/s | - | 8.8 | 24.9 | 48.9 | 26.2 | 0 | - | - |
| P-ChOH | 8.4 | - | - | - | - | - | 6.90 | 0.26 |
| P-ChOH/s | 6.0 | - | - | - | - | - | 17.62 | 0.37 |
| MO-ChOH | - | 5.8 | 24.0 | 50.9 | 25.1 | 0 | - | - |
| MO-ChOH/s | - | 7.8 | 23.1 | 51.9 | 25.0 | 0 | - | - |

The above considerations show clearly that the use of a starch template has a profound impact on the nature of synthesized mixed-oxide catalysts, as it affects the phase composition, the amount of formed spinel, and the crystallinity of the evolving structures.

### 2.1.2. SEM/EDS Analysis

Figures 2–4 show SEM images of the materials obtained with NaOH, TBAOH, and ChOH, respectively. Each set enables the comparison of precursors and calcined samples prepared with or without starch. The common feature of all images is the dominant presence of spherical grains with sizes in the range 2–5 μm, co-existing with a smaller amount of irregular particles of various dimensions. In biotemplated samples, the irregular particles appear larger, both before and after calcination. It is evident that the characteristic features of precursor morphology are retained after calcination. Higher magnification reveals that all grains, independent of their morphology, are, in fact, agglomerates of small particles of ca. 20–50 nm diameter, slightly finer in spheroidal grains. This is illustrated,

in Figure 5, by the example of the P-ChOH/s and MO-ChOH/s samples. The spherical morphology is characteristic of the rhodochrosite phase [23,58]. As to the irregular minority grains, it may be presumed that they are related to the amorphous part of the synthesized materials. This hypothesis is supported by the results of the SEM/EDX compositional analysis of the samples. The result of the SEM/EDX mapping of Cu, Mn, and Al obtained for the MO-ChOH/s sample is shown in Figure 6. It is evident that Mn is preferentially accumulated in spherical agglomerates, as expected for the rhodochrosite-derived phase. Cu and Al contribute to these areas as well, but Mn is the dominating element, as confirmed by point EDX analysis of randomly selected spherules: Mn = 57 at.%, Cu = 23 at.%, and Al = 20 at.% (average of three point analyses). Here, it should be noted that EDX analysis probes a sample depth of the order of 1 μm. This means that point analysis may envelop neighboring particles of different composition; hence, the above values have to be taken as approximates only. For the irregular particle visible in the upper left corner of the SEM image in Figure 6, the relative intensity of Al and Cu mapping is stronger than that of Mn. The enhanced content of Al and Cu suggests that this part of the material stems from the precursor component undetectable by XRD. A point EDX analysis of the irregular agglomerate shows the average contents of Mn, Cu, and Al to be 23, 31, and 46 at.%, respectively. EDX mappings carried out for other samples yield qualitatively similar results, i.e., Cu, Mn, and Al are found in all investigated particles, but the spherical grains are enriched in manganese, while irregular ones accumulate relatively more aluminum and copper.
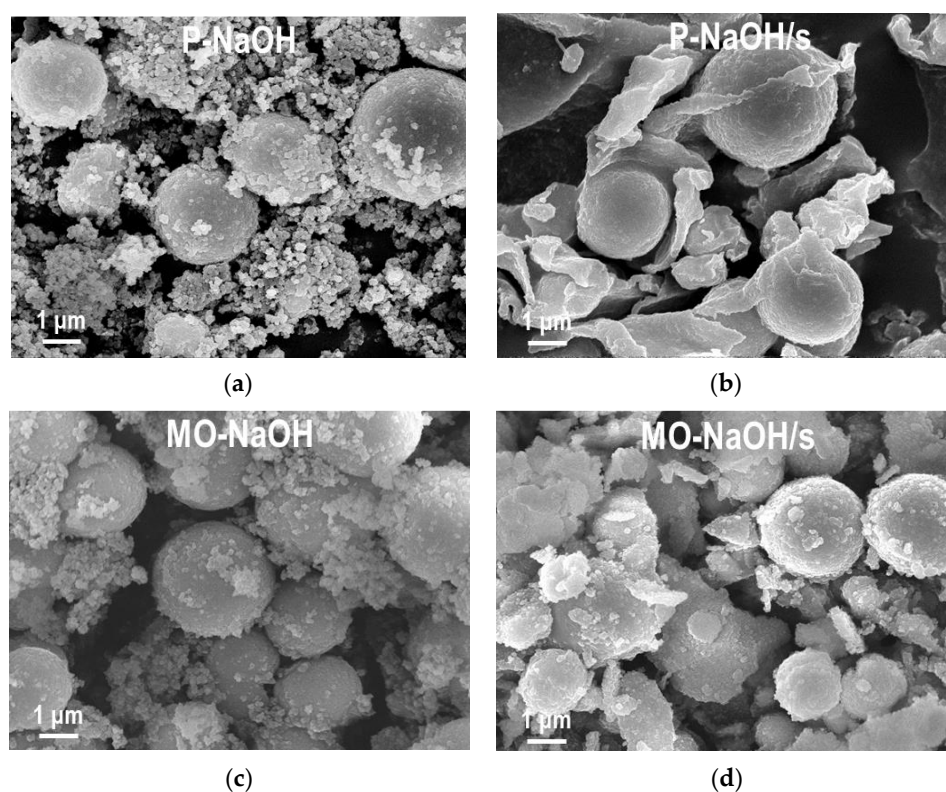


(a)

(b)

(c)

(d)

**Figure 2.** SEM images of precursors and calcined mixed-oxide materials obtained with NaOH precipitant, without or with starch: (**a**) P-NaOH; (**b**) P-NaOH/s; (**c**) MO-NaOH; (**d**) MO-NaOH/s. Magnification ×10,000.
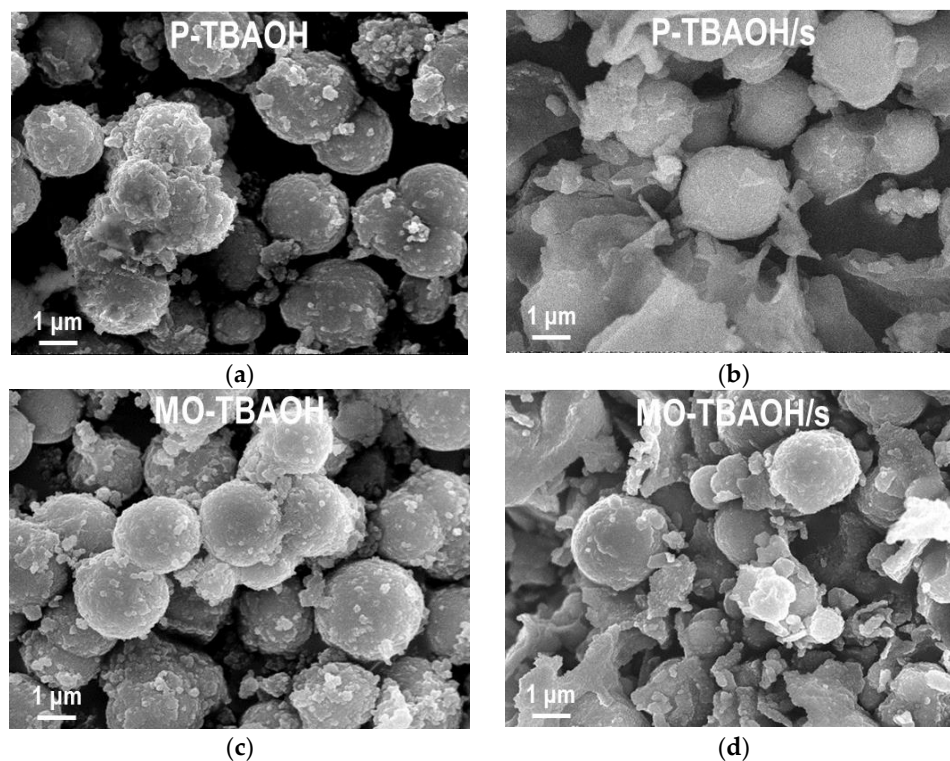
**Figure 3.** SEM images of precursors and calcined mixed-oxide materials obtained with TBAOH precipitant, without or with starch: (**a**) P-TBAOH; (**b**) P-TBAOH/s; (**c**) MO-TBAOH; (**d**) MO-TBAOH/s. Magnification ×10,000.
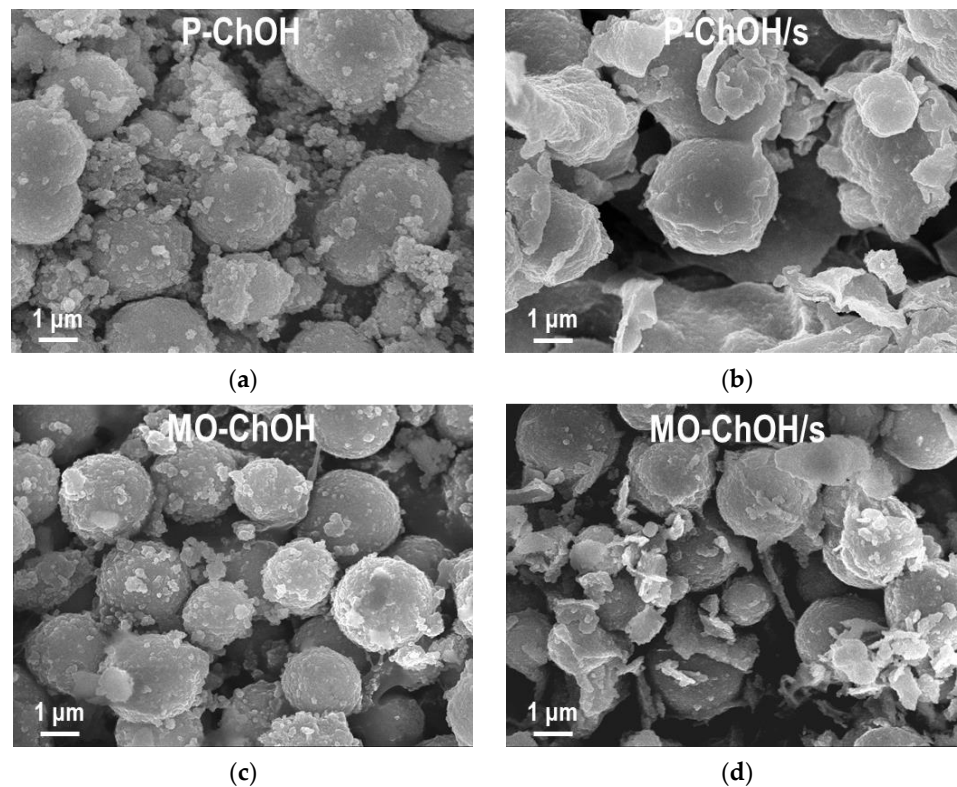


**Figure 4.** SEM images of precursors and calcined mixed-oxide materials obtained with ChOH precipitant, without or with starch: (**a**) P-ChOH; (**b**) P-ChOH/s; (**c**) MO-ChOH; (**d**) MO-ChOH/s. Magnification ×10,000.
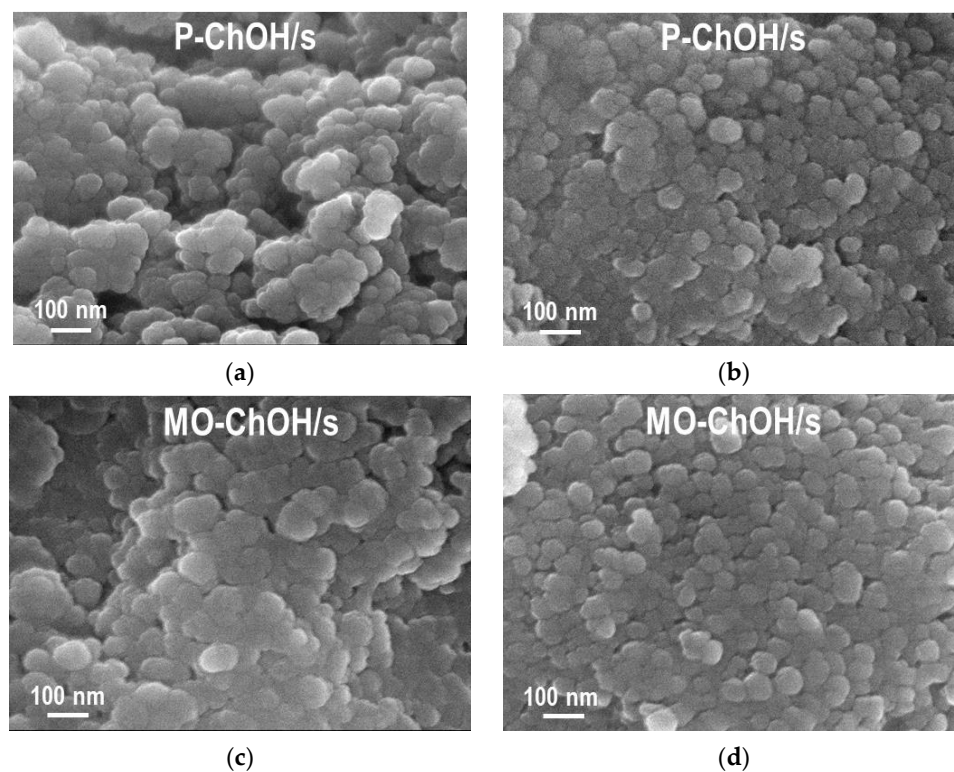
**Figure 5.** High-magnification SEM images of P-ChOH/s precursor and MO-ChOH/s mixed oxides showing close-ups of grains of different morphology: (**a**) P-ChOH/s, surface of irregular agglomerate; (**b**) P-ChOH/s, surface of spheroidal particle; (**c**) MO-ChOH/s, surface of irregular agglomerate; (**d**) MO-ChOH/s, surface of spheroidal particle. Magnification ×100,000.
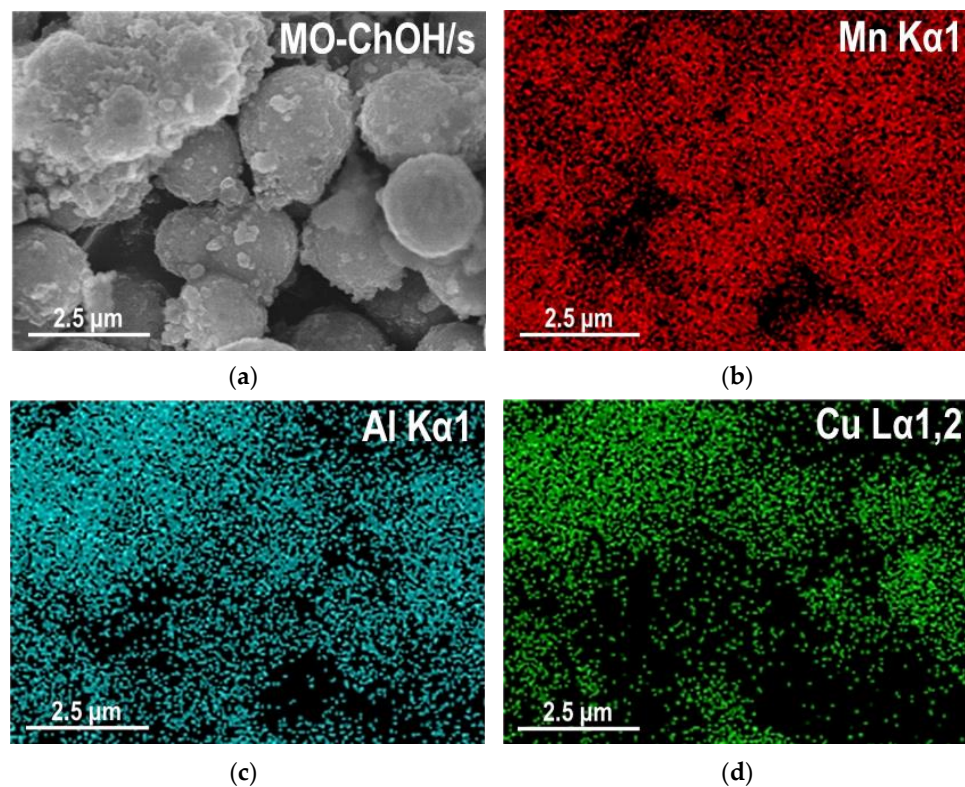


**Figure 6.** SEM/EDX compositional analysis of selected area of MO-ChOH/s sample: (**a**) SEM image; (**b**) EDX mapping image of Mn; (**c**) EDX mapping image of Al; (**d**) EDX mapping image of Cu.

Based on the EDX data, one can conclude that the $Cu_{1.5}Mn_{1.5}O_4$ spinel, the major crystalline phase in the calcined samples, may be present in both types of grains. On the other hand, the amorphous Mn-rich oxide phase, whose presence has been inferred from the XRD data of calcined catalysts, is expected to be located chiefly within the spherical grains, which contain a surplus of Mn with respect to spinel composition. In contrast, in irregular particles, it is copper that is in excess of spinel stoichiometry. Therefore, it may be presumed that crystalline CuO, detected in the biotemplated samples, is present within the irregular agglomerates, intimately intermixed with particles of different composition. Aluminum may contribute to all crystalline and amorphous phases, but it is preferentially located within the irregular agglomerates, most likely as amorphous alumina.

2.1.3. FTIR Analysis

In accordance with the results of the XRD analysis, the FTIR spectra of both series of synthesized solids display bands characteristic of rhodochrosite, marked in Figure 7 by dashed vertical lines. The bands stem primarily from fundamental vibrations of the carbonate anion, i.e., the in-plane symmetric C–O stretching mode ($\nu_1$), the $CO_3$ out-of-plane bending ($\nu_2$), the asymmetric C–O stretching ($\nu_3$), and the in-plane $CO_3$ bending ($\nu_4$) [59]. The wavenumbers determined for each mode are given in the spectrum of P-NaOH. Thus, the low-intensity feature at 1075 cm$^{-1}$ corresponds to $\nu_1$; the sharp, intense band at 861 cm$^{-1}$ is due to $\nu_2$; the broad, intense band at 1452 cm$^{-1}$ stems from $\nu_3$; and the narrow band at 726 cm$^{-1}$ is related to $\nu_4$. It should be noted that in crystalline $MnCO_3$, the carbonate anion has $D_{3h}$ symmetry, and the $\nu_1$ mode is only Raman active. Its activation in the infrared spectrum of the rhodochrosite component formed in the studied precursors points to the lowering of the anion symmetry in the synthesized materials [59–61]. In view of the XRD and SEM/EDS data, the most likely reason for the structural change rendering the $\nu_1$ mode IR active is the incorporation of foreign cations into the $MnCO_3$ lattice. Weak bands visible at 1796 and 2497 cm$^{-1}$ are attributed to the combination of the fundamental modes, namely ($\nu_1 + \nu_4$) and ($\nu_1 + \nu_3$), respectively [61]. A broad maximum around 580 cm$^{-1}$ falls into the range where metal–oxygen and/or metal–hydroxyl bending/librational modes are expected [62]. Its appearance suggests the presence of amorphous hydrotalcites/hydroxides/oxyhydroxides undetected by XRD. Moreover, all samples show a maximum around 3400 cm$^{-1}$, attributed to the stretching modes of O–H bonds, and a band/shoulder at 1630 cm$^{-1}$, due to the bending vibrations of molecular water. The former is slightly red-shifted and has higher intensity in materials precipitated in the presence of starch. The water bending mode is also more intense in biotemplated samples. In addition, all samples are to various degrees contaminated with reactants used for the syntheses. Thus, materials prepared in starch gel display strong bands stemming from this carbohydrate, indicating that remnants of the biotemplate adhere to the precipitated solids. The spectrum of the P-TBAOH sample shows that some TBAOH remained adsorbed at the material's surface, and careful inspection of the P-ChOH spectrum enables the detection of a tiny amount of choline hydroxide residue. The samples also contain different amounts of nitrate impurity, introduced with metal salts and manifested as a characteristic sharp band at 1385 cm$^{-1}$ due to symmetric NO stretching in the $NO_3^-$ anion [62]. The presence of impurities detected in the FTIR spectra was confirmed by the results of the elemental analysis, shown in Table 1. The amount of carbon in CuMn–NaOH is determined by the content of carbonate anions, which are the only source of C in this sample. In all other samples, according to FTIR analysis, there is a contribution of organic carbon, either a major one due to the starch residue or a minor one associated with the remainders of organic bases. The content of analytically determined carbon increases in the following order: P-NaOH < P-ChOH < P-TBAOH << P-NaOH/s < P-ChOH/s < P-TBAOH/s. In the group of samples synthesized without starch, the materials prepared with organic bases show elevated amounts of carbon, which can be assigned to the input of adsorbed ChOH and TBAOH. In the biotemplated samples, the level of carbon is hugely increased, primarily due to the presence of starch residues. However, also here, the samples precipitated with

ChOH and TBAOH show higher C content, pointing to the contribution from the remnants of organic bases. The lowest content of nitrogen is found in NaOH-precipitated solids, in which nitrate anions are the only source of N. The higher amounts of nitrogen found in samples prepared with ChOH and TBAOH are attributed to the residues of the respective quaternary ammonium bases.
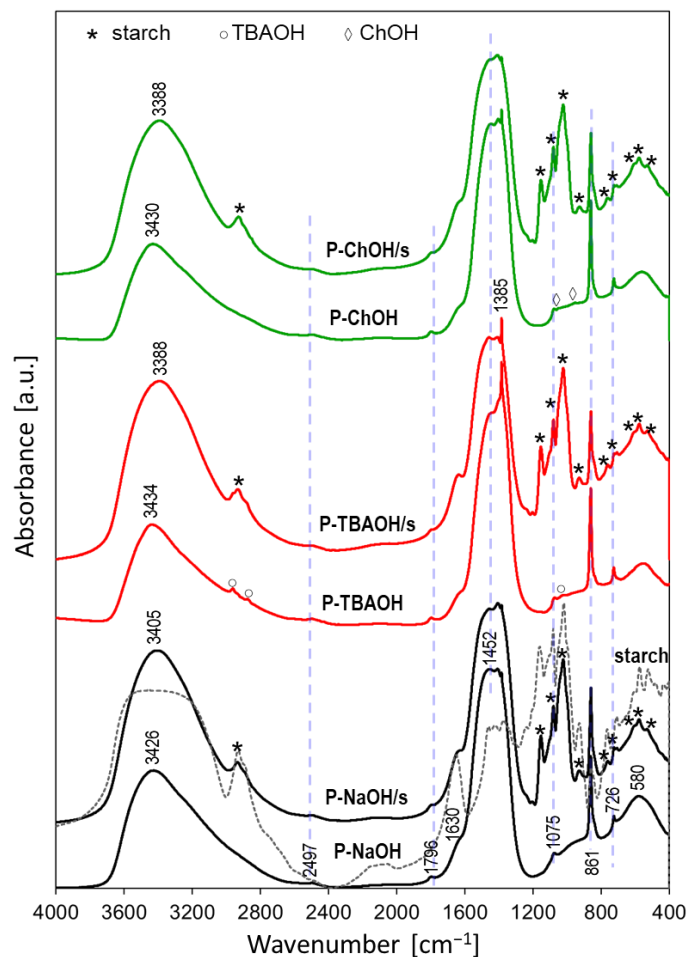


**Figure 7.** FTIR spectra of synthesized precursors (dried starch gel—dashed line).

2.1.4. Thermal Analysis

The results of the TG and DSC analyses of all precursors are shown in Figure 8a,b, respectively. For the sake of comparison, TG and DSC traces obtained for $MnCO_3$ reference are presented as well. Although rhodochrosite is the only crystalline phase visible in the precursors, it is obvious that the TG profiles of the precursors differ significantly from that of the pure $MnCO_3$ phase. The thermal evolution of $MnCO_3$ is consistent with the results of previous studies [63]. This complex process is initiated by the mass loss starting from ca. 100 °C. It is due to the desorption of physisorbed water and/or the departure of water of hydration, retained by $MnCO_3$ precipitated from an aqueous solution. Up to ca. 170 °C, this effect overlaps with the beginning of $MnCO_3$ decomposition and the release of $CO_2$. In the temperature range 170–430 °C, the final release of $CO_2$ takes place; simultaneously, manganese is oxidized to $MnO_2$. Above 430 °C, $MnO_2$ undergoes reduction to $Mn_2O_3$, and the accompanying release of oxygen is responsible for the observed mass loss. The process ends around 540 °C, and the system is stable until about 920 °C, when the next mass loss, due to the reduction of $Mn_2O_3$ to $Mn_3O_4$, occurs. In the DSC trace shown in Figure 8b, only the latter transformation is accompanied by a well-resolved endothermic minimum; other thermal effects are weak and barely discernible. In all precursors, the major mass loss is completed around 350 °C, i.e., nearly 200 °C lower than in pristine $MnCO_3$. The lower

thermal stability of ternary rhodochrosite-like precursors is a consequence of their much poorer crystallinity and the presence of foreign cations in the $MnCO_3$ lattice. The mass loss below 350 °C also encompasses the decomposition of amorphous hydrotalcite-like, hydroxide, and/or carbonate phases present in the precursors. The final small weight loss around 550 °C, which is visible in the TG profiles of all precursors, is a feature known to appear in hydroxycarbonate systems containing copper [20,64,65]. It has been attributed to the release of strongly bound $CO_2$ from amorphous Cu-containing intermediate oxycarbonates. Noteworthily, none of the precursors show the high-temperature weight loss related to the release of oxygen from $Mn_2O_3$ and formation of $Mn_3O_4$, indicating the stabilization of the manganese oxidation state in the mixed-oxide systems formed during the thermal evolution of the precursors. A prominent feature in the TG profiles of the precursors prepared in the presence of starch is a much larger overall weight loss occurring below 350 °C. The effect is accompanied by very strong exothermic effects on the DSC profiles, with two maxima appearing around 250 and 300 °C. In view of the results of the FTIR analysis, which evidence the presence of starch residues in the biotemplated precursors, the phenomena are attributed to the thermal degradation/combustion of starch retained by the precursor precipitates. In the DSC profile of the dried starch gel used in the syntheses (not shown), the exothermic maxima accompanying the weight loss occur at higher temperatures (365 and 480 °C). The observed shift to a lower temperature range is associated with the catalytic action of the Cu–Mn-containing system, which accelerates the combustion of organic residues. Exothermic effects of lower intensity also appear in the samples prepared without starch but with the use of organic bases. The maxima are attributed to the catalytic combustion of the organic remnants, whose presence in the synthesized materials has been evidenced by FTIR spectroscopy.

The results of the thermal analysis provide the rationale for understanding why biotemplated precursors yield a larger amount of spinel phase with better crystallinity in comparison to conventionally prepared counterparts calcined at the same temperature. The key factor is the heat of starch combustion released uniformly in situ within the whole precursor volume. This additional energy input provides conditions for the enhanced formation and crystallization of the spinel phase. Thus, starch residue acts as a fuel in a manner similar to that involved in the combustion syntheses of ceramic nano-powders, which use the highly exothermic ignition of organic compounds to yield well-formed crystalline nanostructured materials [66].

### 2.1.5. $H_2$ TPR-MS Analysis

Reducibility is an important factor influencing the activity of mixed-oxide catalysts in total oxidation reactions. In the present work, it was investigated with the aid of an $H_2$ TPR-MS technique.

The interaction of mixed oxides containing Mn and Cu with hydrogen may involve a number of different redox processes, making the interpretation of results a challenging issue [16,18,21–23,25,30,34,67–72]. In the investigated temperature range, the reduction of $Cu^{2+}$ and/or $Cu^+$ to $Cu^0$, and of $Mn^{4+}$ and/or $Mn^{3+}$ to $Mn^{2+}$, as the final oxidation states, may occur. Moreover, the course of the TPR run depends on many variables, such as the phase composition of mixed oxides, their crystallinity and dispersion, and the initial oxidation states of Cu and Mn. Thus, an overlap of various effects is likely. In the TPR-MS experiments, both $H_2$ uptake and $H_2O$ evolution were followed, enabling additional insight into the nature of prepared mixed oxides. The recorded TPR-MS profiles are presented in Figure 9. It is evident that the overall shape and position of $H_2$ consumption curves vary depending on the presence or absence of starch. Thus, the $H_2$ TPR traces of all mixed oxides derived from precursors synthesized without starch display profiles with two overlapping maxima, around 230 and 270 °C. Such a two-step course of reduction has been observed previously for mixed oxides derived from hydrotalcite precursors synthesized in a similar manner [23]. In this and other works [69,70], the effect at higher temperatures was associated with the reduction of the spinel phase, while the low-temperature maximum was

attributed to the reduction of an amorphous mixed-oxide phase. Such an interpretation is consistent with the results of the present study. Thus, the maxima are better resolved in mixed oxides obtained without the use of starch, which are of poorer crystallinity and richer in the amorphous phase. In all mixed oxides synthesized from biotemplated precursors, the first maximum diminishes and becomes barely visible, while the second one dominates the TPR profile. This effect is in accordance with the structural analysis, which points to the enhanced formation and crystallization of the spinel phase, at the expense of amorphous oxides. Better crystallinity, prompted by the combustion of starch residues, is also the reason for the shift of $H_2$ consumption to higher temperatures.
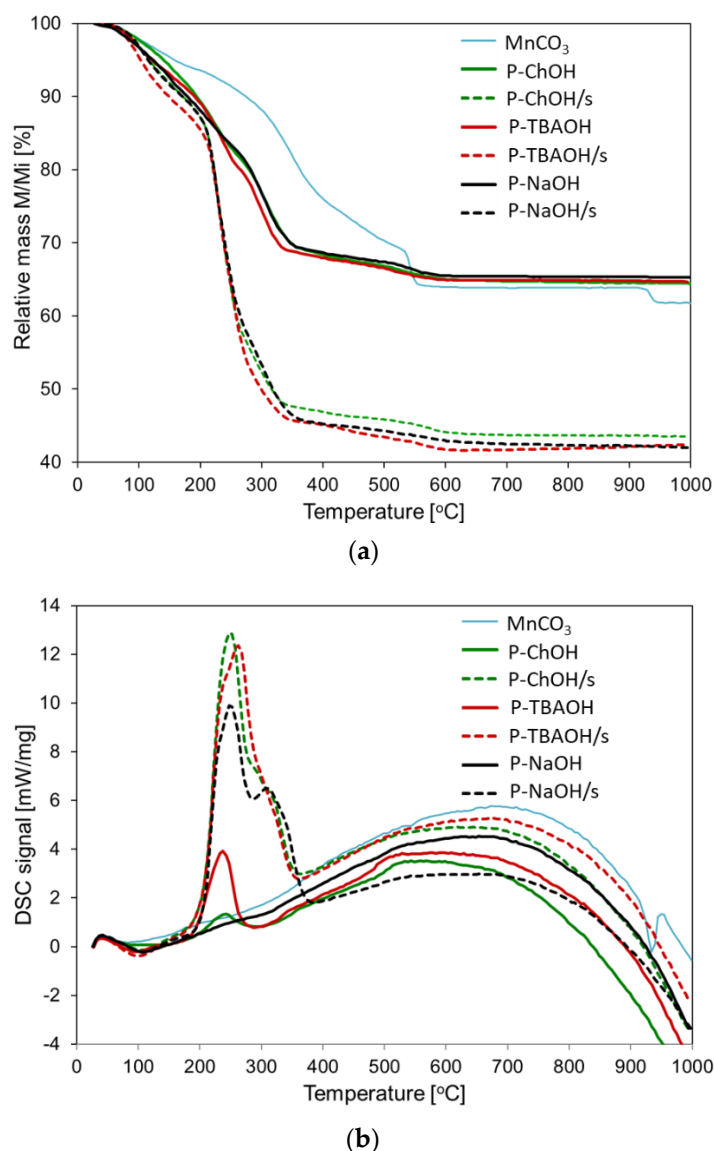


(a)



(b)

**Figure 8.** Thermal analysis of synthesized precursors and of the $MnCO_3$ reference: (**a**) TG profiles; (**b**) DSC profiles.

Analysis of $H_2O$ evolution profiles shows that water is released from the mixed oxides with a delay whose magnitude depends on the manner of synthesis: the effect is less pronounced in samples derived from biotemplated precursors. During the reduction of a mixed-oxide system with hydrogen, the metal cations act as acceptors of electrons while protons react with oxide anions to form hydroxyls. The emission of water results from the subsequent dehydroxylation and is equivalent to the formation of an oxygen vacancy in the oxide sublattice. The data in Figure 9 show that although mixed oxides prepared with

the use of starch are less reducible since they consume hydrogen at higher temperatures than their conventionally co-precipitated counterparts, the difference in the actual lattice oxygen mobility is not so significant, due to the shorter delay in water evolution.
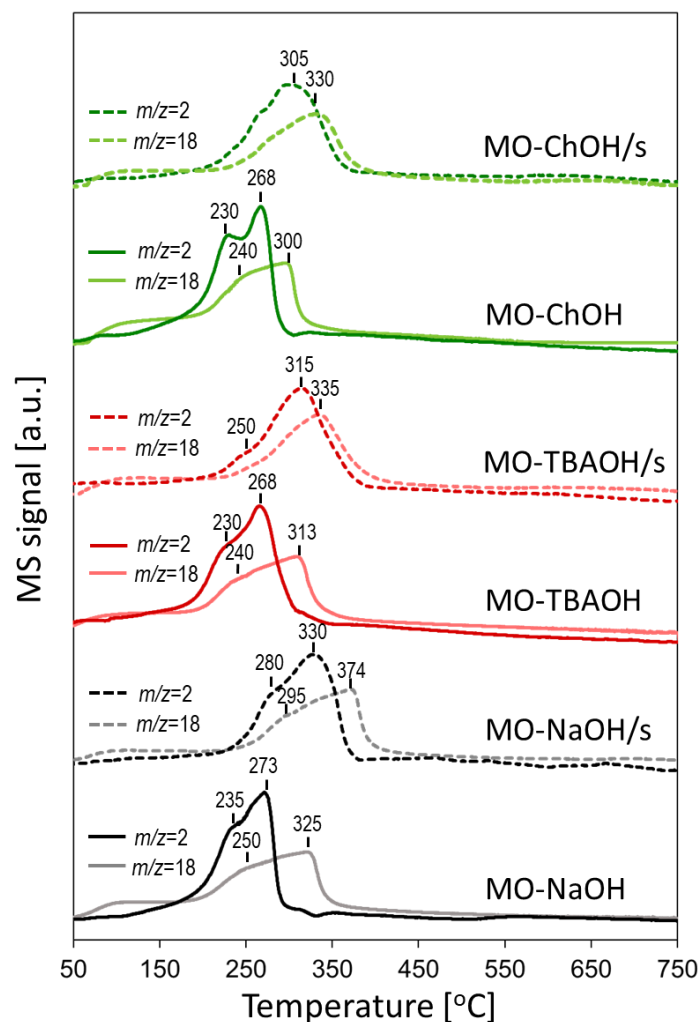


**Figure 9.** TPR-MS profiles of $H_2$ consumption ($m/z = 2$) and $H_2O$ release ($m/z = 18$) by mixed oxides obtained by the calcination of precursors at 450 °C.

## 2.2. Catalytic Combustion of Toluene

Aromatic compounds, such as benzene, toluene, and xylenes, which are collectively known as BTX, are among the most widespread air pollutants. Their emission stems mainly from their use as industrial solvents and from the uncontrolled burning of biomass [7]. In the present work, toluene was chosen as a model VOC for tests of catalyst combustion activity. The temperature dependence of toluene conversion during the catalytic reaction over calcined samples is shown in Figure 10. It is evident that there are differences in catalytic performance, but all materials are very active. Even MO-NaOH, whose conversion vs. temperature profile is most shifted to the high-temperature range, achieves the complete destruction of toluene by 270 °C. In all cases, $CO_2$ was the only carbon-containing product. In order to facilitate the ranking of the catalysts, the $T_{50}$ and $T_{90}$ values, i.e., the temperatures of 50% and 90% toluene conversion, are listed in Table 2. Analysis of the data shows two general trends: (a) all catalysts prepared with the use of a starch template perform better than their conventionally synthesized counterparts, and (b) the catalysts prepared from precursors precipitated with organic bases are more active than those obtained with the use of NaOH.
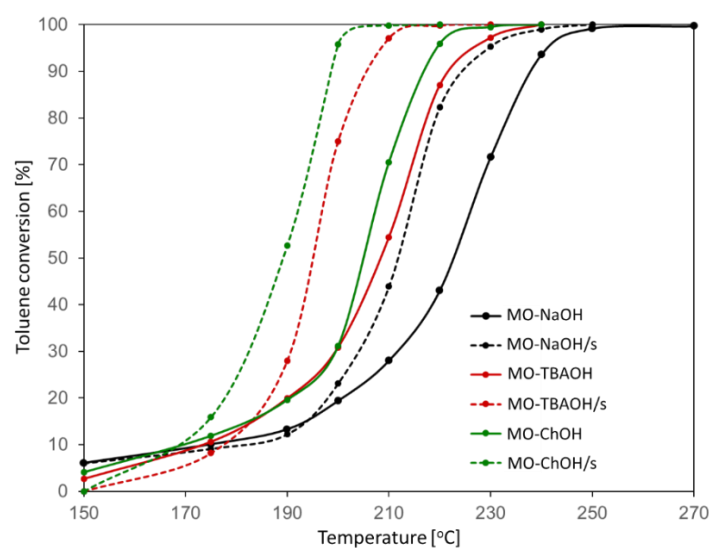
**Figure 10.** Ignition curves for toluene combustion over mixed oxides obtained by the calcination of precursors at 450 °C.

**Table 2.** Temperatures of 50% ($T_{50}$) and 90% ($T_{90}$) conversion of toluene in a reaction of total oxidation over mixed oxides obtained by the calcination of precursors at 450 °C, and the specific surface area of the catalysts ($S_{BET}$).

| Sample | $T_{50}$ [°C] | $T_{90}$ [°C] | $S_{BET}$ [$m^2g^{-1}$] |
|---|---|---|---|
| MO-NaOH | 223 | 238 | 129 |
| MO-NaOH/s | 212 | 224 | 77 |
| MO-TBAOH | 208 | 221 | 161 |
| MO-TBAOH/s | 195 | 205 | 84 |
| MO-ChOH | 205 | 217 | 188 |
| MO-ChOH/s | 189 | 199 | 97 |

The superior performance of catalysts obtained in starch-mediated syntheses is not straightforward to rationalize. The catalytic oxidation of organic compounds over the surface of transition metal oxides usually proceeds via the Mars van Krevelen mechanism [73]. In this mechanism, the reducible metal cations of the catalyst act as actual oxidizing agents, while the lattice oxide anions enter the oxidation product, leaving behind oxygen vacancies. The vacancies are refilled by the ensuing reaction of the catalyst with gaseous oxygen, which simultaneously reinstates the high oxidation state of the cations. Such a transformation is related to the ease with which the catalyst releases the lattice oxygen. In the present work this property is probed by $H_2$ TPR. It is known that oxygen mobility in disordered oxide phases is higher than in well-formed crystalline materials, and, usually, catalysts that are easier to reduce by hydrogen are more active in VOC combustion.

In the present study, the samples prepared in the presence of starch show better crystallinity, and are, therefore, more difficult to reduce. However, contrary to expectations, in the combustion of toluene, the materials perform better than the less-crystalline catalysts synthesized without a biotemplate. As discussed in Section 2.1.5, the difference in the actual lattice oxygen mobility is lesser than suggested by the position of the $H_2$ TPR maxima, due to the shorter delay in water evolution observed in starch-templated samples; however, even the comparison of water evolution profiles points at starch-templated solids as more difficult to reduce. In addition, the catalysts obtained in the presence of starch are characterized by significantly lower specific surface areas than those synthesized in starch-free conditions (Table 2), so their higher activity also contradicts the usually observed trends.

It is proposed that the main reason for the superior activity of starch-templated catalysts is the greater abundance of the $Cu_{1.5}Mn_{1.5}O_4$ spinel phase, evidenced by XRD analysis and TPR data. The key importance of this phase for developing the uniquely high catalytic activity of Cu–Mn mixed-oxide systems in oxidation reactions is widely acknowledged [21–23,30,33,70,74]. The effect is associated with the presence in the spinel structure of two Jahn–Teller ions, namely $Cu^{2+}$ and $Mn^{3+}$, engaged in the reversible redox process: $Cu^{2+} + Mn^{3+} \leftrightarrows Cu^+ + Mn^{4+}$ [57], which is essential for the interaction of the catalyst with the reactants. The increased development of the desired catalytically active phase in MO-NaOH/s, MO-TBAOH/s, and MO-ChOH/s is caused by the presence of starch residue in the respective biotemplated precursors. As argued in Section 2.1.4, the combustion of carbohydrates occurring during the calcination process provides additional heat input, which enhances the formation and crystallization of the $Cu_{1.5}Mn_{1.5}O_4$ spinel phase at the expense of amorphous, non-spinel mixed-oxide components. Besides an increased volume of the spinel phase, yet another factor may contribute to the superior activity of catalysts prepared from starch-templated precursors. XRD analysis demonstrated that the materials also contain, in addition to the spinel phase, a small amount of CuO. Although CuO itself has been repeatedly shown as less active than a mixed Cu–Mn system, it is possible that, at the interface of nanocrystalline CuO and amorphous Mn oxide phases, or CuO and the $Cu_{1.5}Mn_{1.5}O_4$ spinel, active sites are formed that enable efficient hydrocarbon oxidation. The existence of such sites has been proposed for several Cu–Mn oxide systems [29,31,33,36,75,76].

Within a given series of catalysts, the combustion activity follows the order of specific surface areas: MO-NaOH (129 $m^2g^{-1}$) < MO-TBAOH (161 $m^2g^{-1}$) < MO-ChOH (188 $m^2g^{-1}$), and MO-NaOH/s (77 $m^2g^{-1}$) < MO-TBAOH/s (84 $m^2g^{-1}$) < MO-ChOH/s (95 $m^2g^{-1}$). However, the particularly large shifts of ignition curves to higher temperatures, as recorded for MO-NaOH and MO-NaOH/s, suggest that catalyst poisoning with sodium contaminant, present in both samples, may be an additional reason for their poorer performance.

The most active MO-ChOH/s catalyst was subjected to the test of time-on stream stability. The test was carried out by maintaining the catalyst in the reaction flow at 195 °C for over 100 h. Throughout the whole testing time, the toluene conversion remained at the same level of ca. 90%.

The total oxidation of toluene is one of the most studied models of VOC combustion processes because the high production volume and widespread use of this aromatic hydrocarbon make it one of the most prevalent air pollutants. In addition, toluene is highly active in the formation of secondary organic aerosols [2]. There are a number of works reporting the activity of variously prepared mixed Cu–Mn oxide systems in this reaction. Table 3 enables the comparison of some of the published data with the performance of the MO-ChOH/s sample. Despite differences in the experimental conditions, the best catalyst designed in the present work is among the most active Cu–Mn mixed-oxide materials. Bearing in mind that its activity is favorably influenced by the use of a starch-templated precursor, we believe that the simplicity of the synthesis procedure involving starch may serve as an inspiration for the further improvement of other synthetic routes employed in the preparation of this well-researched catalytic system.

**Table 3.** Comparison of literature data on the catalytic combustion of toluene over variously prepared Cu–Mn mixed-oxide catalysts. (WHSV—weight hourly space velocity).

| Reference | $T_{50}$ [°C] | $T_{90}$ [°C] | Toluene Concentration [ppm] | WHSV [$mLg^{-1}h^{-1}$] | $S_{BET}$ [$m^2g^{-1}$] |
|---|---|---|---|---|---|
| Palacio et al. [20] | 258 | n.d. | 800 | 75,000 | 108 |
| Aguilera et al. [21] | 217 | 258 | 1000 | 60,000 | 249 |
| Behar et al. [42] | 239 | n.d. | 1000 | 46,000 | 42 |

**Table 3.** *Cont.*

| Reference | T$_{50}$ [°C] | T$_{90}$ [°C] | Toluene Concentration [ppm] | WHSV [mLg$^{-1}$h$^{-1}$] | S$_{BET}$ [m$^2$g$^{-1}$] |
|---|---|---|---|---|---|
| Kim et al. [71] | 279 | 310 | 1000 | 21,000 | 128 |
| Napruszewska et al. [28] | 261 | 282 | 500 | 20,000 | 273 |
| Wang et al. [30] | 187 | 207 | 500 | 40,000 | 247 |
| Xiao et al. [31] | 228 | 237 | 1000 | 30,000 | 193 |
| Zhang et al. [34] | n.d. | 205 | 1000 | 20,000 | 144 |
| Ye at al. [37] | 202 | 222 | 800 | 30,000 | 105 |
| Li et al. [33] | 207 | 210 | 1000 | 40,000 | 45 |
| Liu et al. [36] | 224 | 234 | 500 | 60,000 | 49 |
| This work | 189 | 199 | 500 | 20,000 | 97 |

## 3. Materials and Methods

### 3.1. Materials

Catalyst precursors were synthesized by co-precipitation at pH = 9, using 1 M aqueous solution of Cu, Mn, and Al nitrates (1:2:1 molar ratio) as the source of metal cations, following the methodology employed previously in the synthesis of Cu–Mn–Al hydrotalcite-like materials [23]. Three different bases were used as precipitating agents: 2 M NaOH, 20 wt. % TBAOH, and 22.5 wt. % ChOH. In the synthesis with NaOH, the carbonate anions were provided by an aqueous solution of $Na_2CO_3$, while in the syntheses with organic bases, $(NH_4)_2CO_3$ was used. The molar content of carbonates was equal to that of Mn. In a typical synthesis, a solution of Cu, Mn, and Al nitrates and a solution of the precipitating agent, contained in respective burettes, were added dropwise to the beaker with a solution of appropriate carbonate, in such a way that the measured pH was kept at a constant level of 9 ($\pm$0.05). All inorganic chemicals used for syntheses were of p.a. purity, purchased from Chempur (Piekary Slaskie, Poland). The 40 wt. % aqueous TBAOH solution was provided by Sigma-Aldrich (Poznan, Poland), and the 45 wt. % ChOH aqueous solution by Acros Organics (Geel, Belgium). The syntheses were performed at room temperature. The precipitates were washed by 3-fold centrifugation with distilled water and freeze-dried. The precursors are further referred to as P-NaOH, P-TBAOH, and P-ChOH. Syntheses of precursors in the presence of a biotemplate were carried out in the same way, except that the water used for the dissolution of reagents was replaced with a gelatinized aqueous solution of starch, prepared by heating a 2 wt. % starch suspension in water at 95 °C for 3 h. Commercial potato starch (PPZ Trzemeszno, Trzemeszno, Poland) was used. The precipitates were washed by 3-fold centrifugation with distilled water and freeze-dried. The samples were denoted P-NaOH/s, P-TBAOH/s, and P-ChOH/s. The reference $MnCO_3$ and Al-doped $MnCO_3$/Al sample were prepared following the same preparative procedure by excluding Cu and Al or Cu nitrates, respectively, from the salt solution. All precursors were subjected to calcination at 450 °C for 3 h to convert them to mixed-oxide catalysts. Calcined mixed-oxide samples obtained without starch are referred to as MO-NaOH, MO-TBAOH, and MO-ChOH, while those prepared in the presence of a biotemplate are denoted MO-NaOH/s, MO-TBAOH/s, and MO-ChOH/s.

### 3.2. Methods

X-ray diffraction (XRD) patterns were obtained with an X'Pert PRO MPD (PANalytical, Almelo, The Netherlands) diffractometer, with Cu K$\alpha$ radiation (40 kV, 30 mA), selected by a flat graphite monochromator, and a step size of 0.0334°. A programmable automated divergence slit giving a constant illuminated sample length of 10 mm was used. The crystal sizes (the sizes of coherently scattering domains) of $MnCO_3$ and spinel phases were estimated with the Scherrer equation from the broadening of the (104) and (400)

reflections, respectively, using the X'Pert High Score software (version 3.0, PANalytical, Almelo, The Netherlands).

Inductively coupled plasma optical emission spectrometry (ICP-OES) was used for the determination of Cu, Mn, Al, and Na. The measurements were carried out by using OPTIMA 2100DV (Perkin-Elmer, Shelton, CT, USA) equipment after the dissolution of samples in a 1:1 (*v/v*) mixture of concentrated HCl and $HNO_3$ acids.

The content of C and N in the samples was determined with the use of an elemental analyzer, i.e., Flash SMART (Thermo Fisher Scientific, Bremen, Germany).

Scanning electron microscopy–energy dispersive X-ray spectroscopy (SEM/EDS) analysis was carried out with the aid of a JEOL JSM-7500F (JEOL, Tokyo, Japan) coupled with an AZtecLiveLite Xplore 30 (Oxford Instruments, Abingdon, UK) system.

Transmission Fourier transform infrared (FTIR) spectra were recorded using a Nicolet 6700 (Thermo Scientific, Madison, WI, USA) spectrometer under atmospheric conditions, in the 4000–400 $cm^{-1}$ range, at a spectral resolution of 2 $cm^{-1}$ for samples prepared as KBr discs.

Combined thermogravimetric (TG) and differential scanning calorimetry (DSC) analyses were carried out in the flow of air (40 mL/min) with an STA 409 PC LUXX TG/DSC apparatus (Netzsch, Selb, Germany), in the temperature range 30–1000 °C, at a heating rate of 10 °C/min.

$H_2$-TPR measurements were performed in a fixed-bed flow reactor connected online to a mass spectrometer (QMG 220 PRISMA PLUS, PFEIFFER, Aßlar, Germany). The signals $m/z = 2$ ($H_2$) and $m/z = 18$ ($H_2O$) were monitored during reduction. For each $H_2$-TPR experiment, 30 mg of sample was loaded into the reactor, and the temperature was increased from RT to 750 °C (ramp 10 °C/min). The reduction was carried out in the flow of 5% $H_2$/Ar (30 mL/min).

The catalytic combustion of toluene was conducted in a fixed-bed flow quartz reactor, using ca. 0.3 g of a catalyst (0.3–0.5 mm fraction) in the temperature range of 150–300 °C. A mixture of 500 ppm of toluene in air was fed to the catalyst at a WHSV of 20,000 $mLg^{-1}h^{-1}$. The only reaction products were $CO_2$ and $H_2O$. Concentrations of toluene and $CO_2$ were analyzed using a Perkin Elmer (Waltham, MA, USA) Clarus 500 gas chromatograph with an Elite-1 30m column, an FID detector, and a methanizer.

## 4. Conclusions

A physicochemical characterization of the materials synthesized in this work shows that catalyst precursors are a mixture of dominant spheroidal, rhodochrosite-like grains with sizes in the range 2–5 μm and minority irregular agglomerates of amorphous phases, most likely of hydrotalcite-like, hydroxide, and/or carbonate type. Both types of grains are built of particles of 20–50 nm size. The morphological characteristics are retained in the calcined solids. Mn, Cu, and Al are present in both types of grains, but the spherical ones contain predominantly Mn, while irregular particles are richer in Cu and Al. The $Cu_{1.5}Mn_{1.5}O_4$ spinel, which is the major crystalline phase in all calcined samples, may be present in both types of grains. The metal elements in excess of the spinel stoichiometry form an amorphous mixed-oxide component. In catalysts derived from starch-templated precursors, small amounts of nanocrystalline CuO are also present.

The precursors prepared in starch gel contain remnants of the biotemplate. Its combustion during calcination prompts the formation of larger amounts of the spinel phase, with better crystallinity in comparison to catalysts prepared from conventionally synthesized precursors.

Tests of toluene combustion show two general trends: a) catalysts prepared with starch perform better than those obtained in starch-free syntheses, and b) catalysts prepared from precursors precipitated with organic bases are more active than those obtained with NaOH. It is proposed that the superior activity of the starch-templated catalysts is chiefly due to the greater abundance of the $Cu_{1.5}Mn_{1.5}O_4$ spinel. The active sites at the interface between nanocrystalline CuO and non-crystalline Mn oxides or between CuO and the $Cu_{1.5}Mn_{1.5}O_4$

spinel may also contribute to the better catalytic activity of these materials. The poorer performance of catalysts obtained from NaOH-precipitated precursors is attributed to the joint effect of the lower specific surface area and poisoning with sodium contaminant.

## References

1. Montero-Montoya, R.; López-Vargas, R.; Arellano-Aguilar, O. Volatile Organic Compounds in Air: Sources, Distribution, Exposure and Associated Illnesses in Children. *Ann. Glob. Health* **2018**, *84*, 225–238. [CrossRef] [PubMed]
2. Kuśtrowski, P.; Rokicińska, A.; Kondratowicz, T. Abatement of volatile organic compounds emission as a target for various human activities including energy production. *Adv. Inorg. Chem.* **2018**, *72*, 385–419.
3. Huang, H.; Xu, Y.; Feng, Q.; Leung, D.Y.C. Low temperature catalytic oxidation of volatile organic compounds: A review. *Catal. Sci. Technol.* **2015**, *5*, 2649–2669. [CrossRef]
4. Krishnamurthy, A.; Adebayo, B.; Gelles, T.; Rownaghi, A.; Rezaei, F. Abatement of Gaseous Volatile Organic Compounds: A Process Perspective. *Catal. Today* **2019**, *350*, 100–119. [CrossRef]
5. He, C.; Cheng, J.; Zhang, X.; Douthwaite, M.; Pattisson, S.; Hao, Z. Recent Advances in the Catalytic Oxidation of Volatile Organic Compounds: A Review Based on Pollutant Sorts and Sources. *Chem. Rev.* **2019**, *119*, 4471–4568. [CrossRef]
6. Lyu, Y.; Li, C.; Du, X.; Zhu, Y.; Zhang, Y.; Li, S. Catalytic removal of toluene over manganese oxide-based catalysts: A review. *Environ. Sci. Pollut. Res.* **2020**, *27*, 2482–2501. [CrossRef]
7. Spivey, J.J. Complete catalytic oxidation of volatile organics. *Ind. Eng. Chem. Res.* **1987**, *26*, 2165–2180. [CrossRef]
8. Everaert, K.; Baeyens, J. Catalytic combustion of volatile organic compounds. *J. Hazard. Mater.* **2004**, *109*, 113–139. [CrossRef]
9. Kamal, M.S.; Razzak, S.A.; Hossain, M.M. Catalytic oxidation of volatile organic compounds (VOCs)—A review. *Atmos. Environ.* **2016**, *140*, 117–134. [CrossRef]
10. Zhang, Z.; Jiang, Z.; Shanguan, W. Low-temperature catalysis for VOCs removal in technology and application: A state-of-the-art review. *Catal. Today* **2016**, *264*, 270–278. [CrossRef]
11. Lee, J.E.; Ok, Y.S.; Tsang, D.C.W.; Song, J.; Jung, S.C.; Park, Y.K. Recent advances in volatile organic compounds abatement by catalysis and catalytic hybrid processes: A critical review. *Sci. Total Environ.* **2020**, *719*, 137405. [CrossRef] [PubMed]
12. Lu, T.; Su, F.; Zhao, Q.; Li, J.; Zhang, C.; Zhang, R.; Liu, P. Catalytic oxidation of volatile organic compounds over manganese-based oxide catalysts: Performance, deactivation and future opportunities. *Sep. Purif. Technol.* **2022**, *396*, 121436. [CrossRef]
13. Lamb, A.B.; Bray, W.C.; Frazer, J.C.W. The Removal of Carbon Monoxide from Air. *J. Ind. Eng. Chem.* **1920**, *12*, 213–221. [CrossRef]
14. Merrill, D.R.; Scalione, C.C. The Catalytic Oxidation of Carbon Monoxide at Ordinary Temperatures. *J. Am. Chem. Soc.* **1921**, *43*, 1982–2002. [CrossRef]
15. Li, W.B.; Chu, W.B.; Zhuang, M.; Hua, J. Catalytic oxidation of toluene on Mn–containing mixed oxides prepared in reverse microemulsions. *Catal. Today* **2004**, *93–95*, 205–209. [CrossRef]
16. Morales, M.R.; Barbero, B.P.; Cadús, L.E. Total oxidation of ethanol and propane over Mn-Cu mixed oxide catalysts. *Appl. Catal. B Environ.* **2006**, *67*, 229–236. [CrossRef]
17. Zimowska, M.; Michalik-Zym, A.; Janik, R.; Machej, T.; Gurgul, J.; Socha, R.P.; Podobiński, J.; Serwicka, E.M. Catalytic combustion of toluene over mixed Cu–Mn oxides. *Catal. Today* **2007**, *119*, 321–326. [CrossRef]
18. Chen, H.; Tong, X.; Li, Y. Mesoporous Cu-Mn Hopcalite catalyst and its performance in low temperature ethylene combustion in a carbon dioxide stream. *Appl. Catal. A Gen.* **2009**, *370*, 59–65. [CrossRef]
19. Vu, V.H.; Belkouch, J.; Ould-Dris, A.; Taouk, B. Removal of hazardous chlorinated VOCs over Mn–Cu mixed oxide based catalyst. *J. Hazard. Mater.* **2009**, *169*, 758–765. [CrossRef]
20. Palacio, L.A.; Velásquez, J.; Echavarría, A.; Faro, A.; Ribeiro, F.R.; Ribeiro, M.F. Total oxidation of toluene over calcined trimetallic hydrotalcites type catalysts. *J. Hazard. Mater.* **2010**, *177*, 407–413. [CrossRef]
21. Aguilera, D.A.; Perez, A.; Molina, R.; Moreno, S. Cu-Mn and Co-Mn catalysts synthesized from hydrotalcites and their use in the oxidation of VOCs. *Appl. Catal. B Environ.* **2011**, *104*, 144–150. [CrossRef]

22. Behar, S.; Gonzalez, P.; Agulhon, P.; Quignard, F.; Świerczyński, D. New synthesis of nanosized Cu-Mn spinels as efficient oxidation catalysts. *Catal. Today* **2012**, *189*, 35–41. [CrossRef]

23. Machej, T.; Serwicka, E.M.; Zimowska, M.; Dula, R.; Michalik-Zym, A.; Napruszewska, B.; Rojek, W.; Socha, R. Cu/Mn-based mixed oxides derived from hydrotalcite-like precursors as catalysts for methane combustion. *Appl. Catal. A Gen.* **2014**, *474*, 87–94. [CrossRef]

24. Behar, S.; Gómez-Mendoza, N.A.; Gómez-García, M.Á.; Świerczyński, D.; Quignard, F.; Tanchoux, N. Study and modelling of kinetics of the oxidation of VOC catalyzed by nanosized Cu-Mn spinels prepared via an alginate route. *Appl. Catal. A Gen.* **2015**, *504*, 203–210. [CrossRef]

25. Tang, W.; Wu, X.; Li, S.; Shan, X.; Liu, G.; Chen, Y. Co-nanocasting synthesis of mesoporous Cu-Mn composite oxides and their promoted catalytic activities for gaseous benzene removal. *Appl. Catal. B Environ.* **2015**, *162*, 110–121. [CrossRef]

26. Wang, H.; Lu, Y.; Han, Y.; Lu, C.; Wan, H.; Xu, Z.; Zheng, S. Enhanced catalytic toluene oxidation by interaction between copper oxide and manganese oxide in Cu-O-Mn/γ-Al$_2$O$_3$ catalysts. *Appl. Surf. Sci.* **2017**, *420*, 260–266. [CrossRef]

27. Ye, Z.; Giraudon, J.M.; Nuns, N.; Simon, P.; De Geyter, N.; Morent, R.; Lamonier, J.F. Influence of the preparation method on the activity of copper-manganese oxides for toluene total oxidation. *Appl. Catal. B Environ.* **2018**, *223*, 154–166. [CrossRef]

28. Napruszewska, B.D.; Michalik, A.; Walczyk, A.; Duraczyńska, D.; Dula, R.; Rojek, W.; Lityńska-Dobrzyńska, L.; Bahranowski, K.; Serwicka, E.M. Composites of Laponite and Cu–Mn Hopcalite-Related Mixed Oxides Prepared from Inverse Microemulsions as Catalysts for Total Oxidation of Toluene. *Materials* **2018**, *11*, 1365. [CrossRef]

29. Luo, M.; Cheng, Y.; Peng, X.; Pan, W. Copper modified manganese oxide with tunnel structure as efficient catalyst for low-temperature catalytic combustion of toluene. *Chem. Eng. J.* **2019**, *369*, 758–765. [CrossRef]

30. Wang, Y.; Yang, D.; Li, S.; Zhang, L.; Zheng, G.; Guo, L. Layered copper manganese oxide for the efficient catalytic CO and VOCs oxidation. *Chem. Eng. J.* **2019**, *357*, 258–268. [CrossRef]

31. Xiao, Z.; Yang, J.; Ren, R.; Li, J.; Wang, N.; Chu, W. Facile synthesis of homogeneous hollow microsphere Cu–Mn based catalysts for catalytic oxidation of toluene. *Chemosphere* **2020**, *247*, 125812. [CrossRef]

32. Solt, H.E.; Németh, P.; Mohai, M.; Sajó;, I.E.; Klébert, S.; Franguelli, F.P.; Fogaca, L.A.; Pawar, R.P.; Kótai, L. Temperature-limited synthesis of copper manganites along the borderline of the amorphous/crystalline state and their catalytic activity in CO oxidation. *ACS Omega* **2021**, *6*, 1523–1533. [CrossRef]

33. Li, J.R.; Zhang, W.P.; Li, C.; He, C. Efficient catalytic degradation of toluene at a readily prepared Mn-Cu catalyst: Catalytic performance and reaction pathway. *J. Coll. Interface Sci.* **2021**, *591*, 396–408. [CrossRef] [PubMed]

34. Zhang, Y.; Zeng, Z.; Li, Y.; Hou, Y.; Hu, J.; Huang, Z. Effect of the A-site cation over spinel AMn$_2$O$_4$ (A = Cu$^{2+}$, Ni$^{2+}$, Zn$^{2+}$) for toluene combustion: Enhancement of the synergy and the oxygen activation ability. *Fuel* **2021**, *288*, 119700. [CrossRef]

35. Ding, S.; Zhu, C.; Hojo, H.; Einaga, H. Enhanced catalytic performance of spinel-type Cu-Mn oxides for benzene oxidation under microwave irradiation. *J. Hazard. Mater.* **2022**, *424*, 127523. [CrossRef]

36. Liu, W.; Xiang, W.; Chen, X.; Song, Z.; Gao, C.; Tsubaki, N.; Zhang, X. A novel strategy to adjust the oxygen vacancy of CuO/MnO$_2$ catalysts toward the catalytic oxidation of toluene. *Fuel* **2022**, *312*, 122975. [CrossRef]

37. Ye, Z.; Giraudon, J.M.; Nuns, N.; Abdallah, G.; Addad, A.; Morent, R.; De Geyter, N.; Lamonier, J.F. Preferential dissolution of copper from Cu-Mn oxides in strong acid medium: Effect of the starting binary oxide to get new efficient copper doped MnO$_2$ catalysts in toluene oxidation. *Appl. Surf. Sci.* **2021**, *537*, 147993. [CrossRef]

38. Herrera-Beurnio, M.C.; Hidalgo-Carrillo, J.; López-Tenllado, F.J.; Martin-Gómez, J.; Estévez, R.C.; Urbano, F.J.; Marinas, A. Bio-Templating: An Emerging Synthetic Technique for Catalysts. A Review. *Catalysts* **2021**, *11*, 1364. [CrossRef]

39. Coelho, A.; Perrone, O.M.; Gomes, E.; Da-Silva, R.; Thoméo, J.C.; Boscolo, M. Mixed metal oxides from sucrose and corn starch templated hydrotalcite-like LDHs as catalysts for ethyl biodiesel synthesis. *Appl. Catal. A* **2017**, *532*, 32–39. [CrossRef]

40. Tao, X.; Liu, D.; Cong, W.; Huang, L. Controllable synthesis of starch-modified ZnMgAl-LDHs for adsorption property improvement. *Appl. Surf. Sci.* **2018**, *457*, 572–579. [CrossRef]

41. Manikandan, M.; Sangeetha, P. Optimizing the Surface Properties of MgO Nanoparticles towards the Transesterification of Glycerol to Glycerol Carbonate. *ChemistrySelect* **2019**, *4*, 6672–6678. [CrossRef]

42. Xiong, Z.; Li, Z.; Li, C.; Wang, W.; Lu, W.; Du, Y.; Tian, S. Green synthesis of Tungsten-doped CeO$_2$ catalyst for selective catalytic reduction of NO with NH$_3$ using starch bio-template. *Appl. Surf. Sci.* **2020**, *536*, 147719. [CrossRef]

43. Michalik, A.; Napruszewska, B.D.; Walczyk, A.; Kryściak-Czerwenka, J.; Duraczyńska, D.; Serwicka, E.M. Synthesis of Nanocrystalline Mg-Al Hydrotalcites in the Presence of Starch—The Effect on Structure and Composition. *Materials* **2020**, *13*, 602. [CrossRef]

44. Karcz, R.; Napruszewska, B.D.; Michalik, A.; Kryściak-Czerwenka, J.; Duraczyńska, D.; Serwicka, E.M. Fine Crystalline Mg-Al Hydrotalcites as Catalysts for Baeyer-Villiger Oxidation of Cyclohexanone with H$_2$O$_2$. *Catalysts* **2021**, *11*, 1493. [CrossRef]

45. Kruissink, E.C.; Pelt, H.L.; Ross, J.R.H.; Van Reüen, L.L. The effect of sodium on the methanation activity of nickel/alumina coprecipitated catalysts. *Appl. Catal.* **1981**, *1*, 23–29. [CrossRef]

46. Liu, W.; Flytzanistephanopoulos, M. Total Oxidation of Carbon Monoxide and Methane over Transition Metal Fluorite Oxide Composite Catalysts. *J. Catal.* **1995**, *153*, 304–316. [CrossRef]

47. Mirzaei, A.A.; Shaterian, H.R.; Joyner, R.W.; Stockenhuber, M.; Taylor, S.H.; Hutchings, G.J. Ambient temperature carbon monoxide oxidation using copper manganese oxide catalysts: Effect of residual Na$^+$ acting as catalyst poison. *Catal. Commun.* **2003**, *4*, 17–20. [CrossRef]

48. Einaga, H.; Maeda, N.; Teraoka, Y. Effect of catalyst composition and preparation conditions on catalytic properties of unsupported manganese oxides for benzene oxidation with ozone. *Appl. Catal. B Environ.* **2013**, *142–143*, 406–413. [CrossRef]

49. Castañeda, R.; Pascual, L.; Martínez-Arias, A. Influence of sodium impurities on the properties of $CeO_2/CuO$ for carbon monoxide oxidation in a hydrogen-rich stream. *Catal. Commun.* **2018**, *108*, 88–92. [CrossRef]

50. Einaga, H.; Kiya, A.; Yoshioka, S.; Teraoka, Y. Catalytic properties of copper–manganese mixed oxides prepared by coprecipitation using tetramethylammonium hydroxide. *Catal. Sci. Technol.* **2014**, *4*, 3713–3722. [CrossRef]

51. Shuck, C.E.; Ventura-Martinez, K.; Goad, A.; Uzun, S.; Shekhirev, M.; Gogotsi, Y. Safe Synthesis of MAX and MXene: Guidelines to Reduce Risk During Synthesis. *ACS Chem. Health Saf.* **2021**, *28*, 326–338. [CrossRef]

52. Karcz, R.; Napruszewska, B.D.; Walczyk, A.; Kryściak-Czerwenka, J.; Duraczyńska, D.; Płaziński, W.; Serwicka, E.M. Comparative Physicochemical and Catalytic Study of Nanocrystalline Mg-Al Hydrotalcites Precipitated with Inorganic and Organic Bases. *Nanomaterials* **2022**, *12*, 2775. [CrossRef] [PubMed]

53. Bukhtiyarova, M.V. A review on effect of synthesis conditions on the formation of layered double hydroxides. *J. Solid State Chem.* **2019**, *269*, 494–596. [CrossRef]

54. Porta, P.; Moretti, G.; Jacono, M.L.; Musicanti, M.; Nardella, A. Characterization of copper–manganese hydroxysalts and oxysalts. *J. Mater. Chem.* **1991**, *1*, 129–135. [CrossRef]

55. Clarke, T.J.; Davies, T.E.; Kondrat, S.A.; Taylor, S.H. Mechanochemical synthesis of copper manganese oxide for the ambient temperature oxidation of carbon monoxide. *Appl. Catal. B Environ.* **2015**, *165*, 222–231. [CrossRef]

56. Fubini, B.; Stone, F.S. Physico-chemical properties of $MnCO_3$–$CaCO_3$ and $MnO$–$CaO$ solid solutions. *J. Chem. Soc. Faraday Trans.* **1983**, *79*, 1215. [CrossRef]

57. Gillot, B.; Buguet, S.; Kester, E. Oxidation mechanism and valence states of copper and manganese in tetragonal $CuMn_2O_4$. *J. Mater. Chem.* **1997**, *7*, 2513–2517. [CrossRef]

58. Garcia, J.C.; Barai, P.; Chen, J.; Gutierrez, A.; Wen, J.; Arslan, I.; Wang, X.; Fister, T.T.; Iddir, H.; Srinivasan, V. Predicting Morphological Evolution during Coprecipitation of $MnCO_3$ Battery Cathode Precursors Using Multiscale Simulations Aided by Targeted Synthesis. *Chem. Mater.* **2020**, *32*, 9126–9139. [CrossRef]

59. Busca, G.; Lorenzelli, V. Infrared spectroscopic identification of species arising from reactive adsorption of carbon oxides on metal oxide surfaces. *Mater. Chem.* **1982**, *7*, 89–126. [CrossRef]

60. Andersen, F.A.; Brečević, L. Infrared spectra of amorphous and crystalline calcium carbonate. *Acta Chem. Scand.* **1991**, *45*, 1018–1024. [CrossRef]

61. Boulard, E.; Goncharov, A.F.; Blanchard, M.; Mao, W.L. Pressure-induced phase transition in $MnCO_3$ and its implications on the deep carbon cycle. *J. Geophys. Res. Solid Earth* **2015**, *120*, 4069–4079. [CrossRef]

62. Kagunya, W.; Baddour-Hadjean, R.; Kooli, F.; Jones, W. Vibrational modes in layered double hydroxides and their calcined derivatives. *Chem. Phys.* **1998**, *236*, 225–234. [CrossRef]

63. Biernacki, L.; Pokrzywnicki, S. The Thermal Decomposition of Manganese Carbonate. Thermogravimetry and Exoemission of Electrons. *J. Therm. Anal. Calorim.* **1999**, *55*, 227–232. [CrossRef]

64. Velu, S.; Swamy, C.S. Synthesis and physicochemical properties of a new copper-manganese-aluminium ternary hydrotalcite-like compound. *J. Mater. Sci. Lett.* **1996**, *15*, 1674–1677. [CrossRef]

65. Kovanda, F.; Grygar, T.; Dorničák, V.; Rojka, T.; Bezdička, P.; Jirátová, K. Thermal behaviour of Cu–Mg–Mn and Ni–Mg–Mn layered double hydroxides and characterization of formed oxides. *Appl. Clay Sci.* **2005**, *28*, 121–136. [CrossRef]

66. Mukasyan, A.S.; Rogachev, A.S.; Aruna, S.T. Combustion synthesis in nanostructured reactive systems. *Adv. Powder Technol.* **2015**, *26*, 954–976. [CrossRef]

67. Tanaka, Y. Water gas shift reaction for the reformed fuels over Cu/MnO catalysts prepared via spinel-type oxide. *J. Catal.* **2003**, *215*, 271–278. [CrossRef]

68. Saqer, S.M.; Kondarides, D.I.; Verykios, X.E. Catalytic oxidation of toluene over binary mixtures of copper, manganese and cerium oxides supported on γ-$Al_2O_3$. *Appl. Catal. B Environ.* **2011**, *103*, 275–286. [CrossRef]

69. Hosseini, S.A.; Niaei, A.; Salari, D.; Alvarez-Galvan, M.C.; Fierro, J.L.G. Study of correlation between activity and structural properties of Cu-(Cr, Mn and Co)$_2$ nano mixed oxides in VOC combustion. *Ceram. Int.* **2014**, *40*, 6157–6163. [CrossRef]

70. Papavasiliou, J.; Avgouropoulos, G.; Ioannides, T. Combined steam reforming of methanol over Cu–Mn spinel oxide catalysts. *J. Catal.* **2007**, *251*, 7–20. [CrossRef]

71. Kim, S.C.; Park, Y.K.; Nah, J.W. Property of a highly active bimetallic catalyst based on a supported manganese oxide for the complete oxidation of toluene. *Powder Technol.* **2014**, *266*, 292–298. [CrossRef]

72. Jabłońska, M.; Chmielarz, L.; Węgrzyn, A.; Góra-Marek, K.; Piwowarska, Z.; Witkowski, S.; Bidzińska, E.; Kuśtrowski, P.; Wach, A.; Majda, D. Hydrotalcite derived (Cu, Mn)–Mg–Al metal oxide systems doped with palladium as catalysts for low-temperature methanol incineration. *Appl. Clay Sci.* **2015**, *114*, 273–282. [CrossRef]

73. Valange, S.; Védrine, J. General and Prospective Views on Oxidation Reactions in Heterogeneous Catalysis. *Catalysts* **2018**, *8*, 483. [CrossRef]

74. Liu, T.; Yao, Y.; Wei, L.; Shi, Z.; Han, L.; Yuan, H.; Li, B.; Dong, L.; Wang, F.; Sun, C. Preparation and Evaluation of Copper–Manganese Oxide as a High-Efficiency Catalyst for CO Oxidation and NO Reduction by CO. *J. Phys. Chem. C* **2017**, *121*, 12757–12770. [CrossRef]

75.  Liu, X.S.; Jin, Z.N.; Lu, J.Q.; Wang, X.X.; Luo, M.F. Highly active CuO/OMS-2 catalysts for low-temperature CO oxidation. *Chem. Eng. J.* **2010**, *162*, 151–157. [CrossRef]
76.  Liu, B.; Wu, H.; Li, S.; Xu, M.; Cao, Y.; Li, Y. Solid-State Construction of CuOx/Cu$_{1.5}$Mn$_{1.5}$O$_4$ Nanocomposite with Abundant Surface CuO$_x$ Species and Oxygen Vacancies to Promote CO Oxidation Activity. *Int. J. Mol. Sci.* **2022**, *23*, 6856. [CrossRef]